NANO · MICRO small
www.small-journal.com

Liquid Processing of Interfacially Grown Iron-Oxide Flowers into 2D-Platelets Yields Lithium-Ion Battery Anodes with Capacities of Twice the Theoretical Value

Bharathi Konkena, Harneet Kaur, Ruiyuan Tian, Cian Gabbett, Mark McCrystall, Dominik Valter Horvath, Kevin Synnatschke, Ahin Roy, Ross Smith, Valeria Nicolosi, Micheál D. Scanlon, and Jonathan N. Coleman**

Iron oxide (Fe_2O_3) is an abundant and potentially low-cost material for fabricating lithium-ion battery anodes. Here, the growth of α-Fe_2O_3 nano-flowers at an electrified liquid–liquid interface is demonstrated. Sonication is used to convert these flowers into quasi-2D platelets with lateral sizes in the range of hundreds of nanometers and thicknesses in the range of tens of nanometers. These nanoplatelets can be combined with carbon nanotubes to form porous, conductive composites which can be used as electrodes in lithium-ion batteries. Using a standard activation process, these anodes display good cycling stability, reasonable rate performance and low-rate capacities approaching 1500 mAh g^{-1}, consistent with the current state-of-the-art for Fe_2O_3. However, by using an extended activation process, it is found that the morphology of these composites can be significantly changed, rendering the iron oxide amorphous and significantly increasing the porosity and internal surface area. These morphological changes yield anodes with very good cycling stability and low-rate capacity exceeding 2000 mAh g^{-1}, which is competitive with the best anode materials in the literature. However, the data implies that, after activation, the iron oxide displays a reduced solid-state lithium-ion diffusion coefficient resulting in somewhat degraded rate performance.

1. Introduction

Lithium-ion batteries (LIB) are very widely used for energy storage in portable electronic devices and increasingly for electric vehicles.[1] Even after 30 years, LIBs are undergoing constant renewal, for example via the commercialization of new electrode materials. To date, a range of anode materials, from commonly-used graphite (theoretical capacity of 379 mAh g^{-1}) to the current state-of-the-art, silicon (theoretical capacity of 3500 mAh g^{-1}), have been used to improve performance.[2,3] However, the commercial implementation of new materials is often hampered by insufficient cycling stability, poor rate performance at high currents and large voltage hysteresis, as well as an inability to meet ever-increasing energy/power demands.[4,5] While silicon is a very promising high capacity, energy-efficient and environment-friendly anode material, it is still worth exploring alternative anode materials which might have specific advantages, for example in terms of cost.

Transition metal compounds, such as transition metal oxides (TMO), sulfides, fluorides, phosphides and nitrides, have large theoretical lithium-storing capacities (generally from 500 to 1500 mAh g^{-1}), which are generally associated with conversion and/or alloy type reactions.[5–7] These conversion type anode materials are known to exhibit additional reversible capacity exceeding their (already high) theoretical capacity through mechanisms that are still poorly understood.[8,9] In particular, while hematite (α-Fe_2O_3) has a theoretical capacity of 1007 mAh g^{-1}, it has been reported to deliver reversible capacities of up to 2000 mAh g^{-1}, higher than other conversion type anodes.[10–14] However, such conversion electrodes can suffer from poor cycling stability and large voltage hysteresis, which degrade the electrode rate performance.[15,16] Nevertheless, composite electrodes based on Fe_2O_3 have demonstrated reasonable rate performance to facilitate fast charging or high-power output.[10]

It is well known that the nanosizing of active particles can yield significant advantages in terms of achieved capacity and rate performance.[17] In the case of layered materials, multiple

B. Konkena, H. Kaur, R. Tian, C. Gabbett, M. McCrystall, D. V. Horvath, K. Synnatschke, R. Smith, J. N. Coleman
School of Physics
CRANN & AMBER Research Centres
Trinity College Dublin
Dublin D02 PN40, Ireland
E-mail: colemaj@tcd.ie
A. Roy, V. Nicolosi
School of Chemistry
CRANN & AMBER Research Centres
Trinity College Dublin
Dublin D02 PN40, Ireland
M. D. Scanlon
The Bernal Institute and Department of Chemical Sciences
University of Limerick
Limerick V94 T9PX, Ireland
E-mail: micheal.scanlon@ul.ie
The ORCID identification number(s) for the author(s) of this article can be found under https://doi.org/10.1002/smll.202203918.

DOI: 10.1002/smll.202203918

papers have shown that converting bulk powder to 2D nanosheets yields significant capacity increases.[18–20] In addition, 2D platelet-shaped nanoparticles show great potential for use in battery electrodes due to shorter solid state diffusion lengths which can yield improved rate performance.[21] However, high aspect ratio 2D nanosheets can reduce the diffusion coefficient associated with ion transport within the electrolyte filled pores.[21] To avoid slow liquid phase diffusion while maintaining short solid state diffusion times, quasi-2D platelets with reduced aspect ratio are required.[21] This suggests that when using Fe_2O_3 for battery applications there would be significant advantages to producing it in the form of quasi-2D platelets.

Several synthetic routes have been proposed to generate nanoscale α-Fe_2O_3 of various geometries including 2D platelets.[22–25] However, current methods are expensive to implement and typically include multiple complex steps which require high temperatures as well as templates or solid supports. A simpler alternative is to use a controllable, soft interfacial method to self-assemble well-defined and mesoporous nanostructures at an immiscible aqueous/organic interface.[26] The interface provides a defect-free, dimensionally-confined space to self-assemble unique 2D nanomaterials in a single step with perfect reproducibility. This can yield nanomaterials, potentially including quasi-2D materials, that are inaccessible in bulk solution.[27,28] Furthermore, certain interfaces between two immiscible electrolyte solutions (ITIES) may be electrochemically polarized, providing a driving force that may influence the kinetics of self-assembly or even enable electrosynthesis of interfacial thin films of materials.[29,30]

Another consideration involves electrode architecture and the need to include conductive additives. For Fe_2O_3, a number of carbon-based additives including 2D graphene, 1D carbon (nanofibers/nanotubes), and 0D nanocarbon has been extensively explored.[10,31–34] We believe significant advantages are to be had from using carbon nanotubes (CNTs) as the conductive additive. We and others have shown that incorporating CNTs in electrodes based on both 2D[35–37] and 3D[38] materials allows them to approach their theoretical capacity. This is because the high conductivity of the CNTs allows effective charge distribution increasing both initial capacity, stability, and rate performance.[38–40] In addition, CNTs provide mechanical reinforcement to the electrode without the need for any additional binder.[38] This is particularly important for iron oxide-based anodes, where a large volume expansion is often observed upon lithiation which leads to particle de-cohesion and poor cycling performance.[7] We have shown previously that nanotubes lead to electrode toughening which imparts stability even in silicon anodes which display very high volume expansion.[38]

In this paper we will combine the advantages associated with quasi-2D Fe_2O_3 as an active material with those of using CNTs as both conducting additive and binder. We demonstrate the use of interfacial synthesis at a polarized ITIES to prepare easily reproducible and scalable α-Fe_2O_3 flower like sheet-based structures. These interfacially grown α-Fe_2O_3 flowers are then converted to quasi-2D platelets by sonication and mixed with CNTs to form a conductive composite for use in a Li-storing anode. After extended activation, we obtain a very high specific capacity for α-Fe_2O_3/CNT thin film electrodes of 2115 mA h g^{-1} after 345 cycles with 100% coulombic efficiency as well as good rate capability and cycling performance.

2. Experimental Section

2.1. Interfacial Synthesis Fe_2O_3 Microstructures at a Polarized Aqueous/Organic Interface

Interfacial synthesis was carried out at an interface between two ITIES, formed between an acidic aqueous solutions containing lithium perchlorate (0.1 M $LiClO_4$) electrolyte and 0.25 mM of $FeCl_2$ as the oxidant, and an organic 1,2-DCE solution containing tetrabutylammonium perchlorate (0.1 M $TBAClO_4$) electrolyte and 0.25 mM of 4-aminopyridine as a ligand. In a typical experiment, the interfacial electric potential difference at an aqueous/DCE interface ($\Delta_o^w\phi$) was established using ClO_4^- as a common ion. ClO_4^- has a high tendency to transfer ligands in the organic phase to the aqueous phase and, therefore, contributes to a higher driving force to push 4-aminopyridine ligand to react with Fe^{2+} in the aqueous solution. This biphasic system was left for ≈12 h at room temperature during which the reactants diffused toward the interface. In the next step, nucleation and growth of Fe_2O_3 particles led to the assembly of the individual flakes at the ITIES, and dark green colored material assembled at the liquid/liquid interface, covering the whole interface (see **Figure 1**B). Later both aqueous and organic phases were removed successively, the precipitate was collected and washed with a mixture of absolute ethanol and distilled water several times to remove the solvents effectively, was subsequently dried in an oven at 80 °C overnight, and the resultant powder was brown in color. Finally, the red colored powder was obtained after calcinating the dried powder at 350 °C for 3 h (Figure 1C).

2.2. Liquid Processing of IG-α-Fe_2O_3 into 2D-Platelets

The α-Fe_2O_3 dispersion with an initial concentration of 2.5 g L^{-1} was prepared by adding 200 mg powder to 80 mL of N-methyl-2-pyrrolidon (NMP) (Sigma Aldrich HLPC grade ≥ 99%) in a metallic beaker and then probe sonicating (tapered tip, VibraCell CVX, 750 W) for 6 h at a pulse of 6 s on and 2 s off 6 with an amplitude of 45%, under ice cooling. The resultant dispersion was centrifuged in a Hettich Mikro 220R centrifuge equipped with a fixed-angle rotor 1016 at 26 g for 2 h and the sediment containing the large unexfoliated material was discarded, while the supernatant with exfoliated sheets were further subjected to a second centrifugation at 2600 g for 2 h. The resultant supernatant containing very small particles was discarded, and the sediment was redispersed in (5 mL) isopropyl alcohol (IPA) to give a standard sample trapped between 0.026 and 2.6 kg consisting of polydisperse nanosheets.

2.3. Characterization

A Horiba Jobin-Yvon LabRAM HR800 was used to acquire the Raman spectra with a 633 nm excitation laser in air under

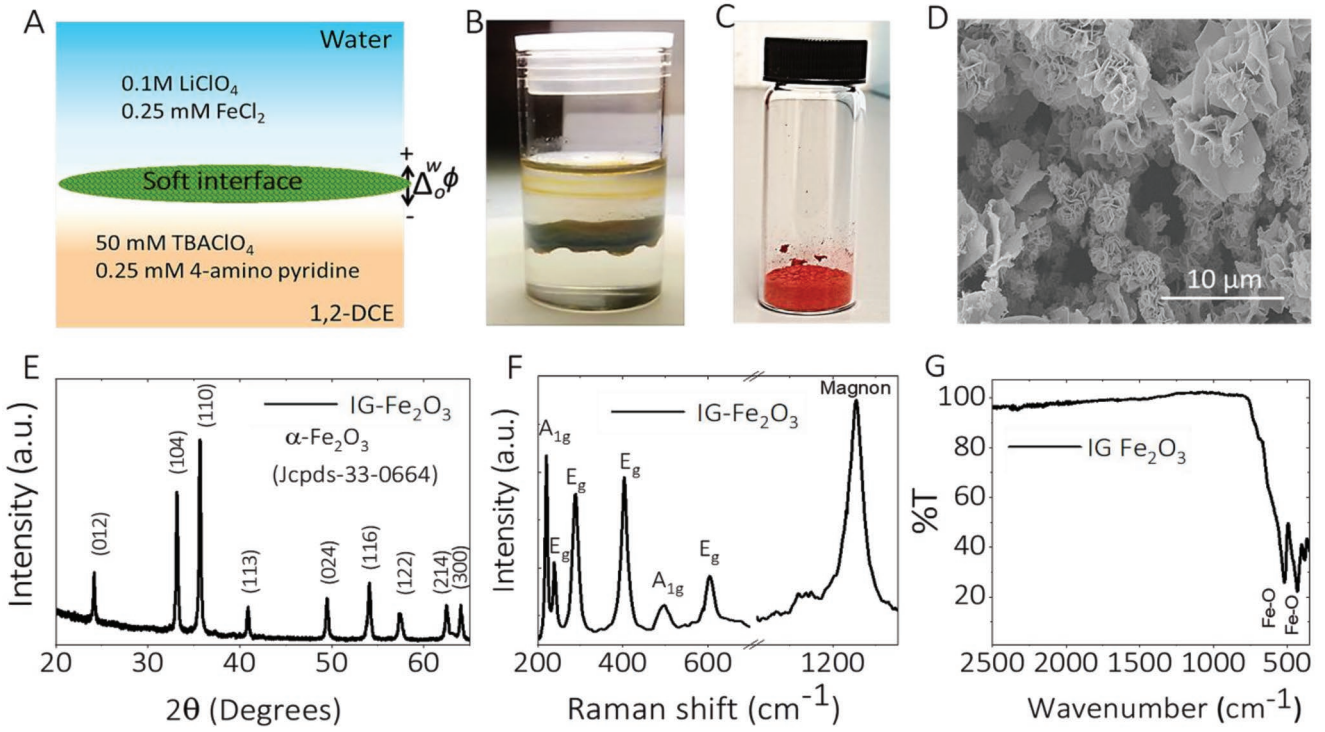

Figure 1. Interfacial synthesis and structural characterization of α-Fe_2O_3 micro-structures. A) Schematic representation of interfacial synthesis at the interface between two immiscible electrolyte solutions (ITIES). B) Photograph of the assembled iron oxide layer at the ITIES after 12 h of reaction. C) Iron oxide powder obtained from the interfacial synthesis after annealing at 350 °C for 3 h. D) SEM image of interfacial grown iron oxide powder shows presence of randomly assembled 3D flower-like microstructures. E) X-ray diffraction pattern of the interfacial grown α-Fe_2O_3. The diffraction peaks at 24.1°, 33.1°, 35.6°, 40.8°, 49.5°, 54.1°, 57.6°, 62.5° and 64.0° corresponded to (012), (104), (110), (113), (024), (122), (116), (214) and (300) planes of the rhombohedral crystal lattice structure of α-Fe_2O_3, space group R3-c (reference, JCPDS 00-33-0664). F) Raman-scattering spectrum of interfacial grown α-Fe_2O_3 micro-structures. G) FTIR spectra of as-synthesized α-Fe_2O_3 micro-structures.

ambient conditions. Laser spot on the sample was focused in 2 µm with 0.2 mW power. Scattered light was collected by a long working distance objective with a magnification of 100×. A diffraction grating of 600 grooves was chosen, obtaining ≈1.5 cm^{-1} spectral resolution. Each spectrum is the average of 16 different spectra and each of them integrated for 30 s. Measurements were performed on powdered IG-Fe_2O_3 and a thin film of standard Fe_2O_3 dispersion was obtained by drop-cast. Optical spectra were measured using a Perkin Elmer Lambda 1050 UV–visible spectrometer with a silica glass cuvette (path length 4 mm). The spectrometer was equipped with an integrating sphere for measuring the absorption where scattering effects were removed.

Liquid dispersions (15 µL) of size-selected samples were diluted until transparent and drop-cast onto preheated (100 °C) Si/SiO_2 (300 nm oxide layer) wafers. AFM was subsequently carried out on a Bruker Multimode 8 microscope in ScanAsyst mode with Oltespa R3 cantilevers. In preparation for TEM imaging, the standard dispersion was diluted to optical transparency and manually drop-cast one drop at a time onto a holey carbon TEM grid with the aim of dropping ≈0.1 mg of material. The grids were left to dry in air and then placed overnight in a vacuum oven at 70 °C to dry completely before measuring. Bright-field TEM imaging was performed using a JEOL 2100 microscope. EDX spectroscopy was performed in situ with TEM imaging using an 80 mm^2 XMAX EDX detector.

The SEM images of as synthesized Fe_2O_3 powder, the prepared Fe_2O_3, and Fe_2O_3/CNT composite films were obtained using a Zeiss Ultra Plus SEM. Accelerating voltages of 2–5 kV, with a 30 µm aperture at a working distance of 3–6 mm, were used. The pure Fe_2O_3 and the Fe_2O_3/CNT composite films were imaged on the polymer filtration membrane. To minimize charging, the sides of the samples were coated with silver paint. Furthermore, the Fe_2O_3/CNT composite films were snapped at room temperature, and the fractured sides were looked at for the cross-sectional images.

2.4. Electrochemical Characterization

SWCNT dispersions with a concentration of 0.1 mg mL^{-1} were prepared by adding 8 mg P3-SWCNT to 80 mL IPA and sonicating for 2 h using a horn-tip sonic probe (Vibracell CVX, 750 W) at 50% amplitude with an on/off pulse ratio of 6 s/2 s. To fabricate electrodes, the Fe_2O_3 dispersions were mixed with CNT (75:25 in weight) dispersions in IPA and vacuum filtered on Celgard 2320 (thickness 20 µm) membrane with an area of 2 cm^2, the composite electrode referred as Fe_2O_3/CNT throughout the manuscript. The SWCNT were used to maximize both the mechanical stability and electrical conductivity of the resulting films and were the only additives used. The resulting films were cut into the required dimensions for

electrochemical testing (A = 0.178 cm^2). The areal mass loadings of Fe_2O_3 in electrodes were 0.6–0.7 mg cm^{-2}, with 30 wt% SWCNT and approximate thicknesses 5–6 µm.

Coin cells were assembled (2032 type, 14 mm; MTI Corp.) in a glovebox filled with O_2 and H_2O content lower than 0.1 ppm and tested at room temperature. Li-metal disc used as the counter/reference electrode, while Celgard C2320 (thickness 20 µm) was used as a separator. Lithium hexafluorophosphate (LiPF6, 1.2 M) in ethylene carbonate/ethyl methyl carbonate (EC/EMC, 1:1 in vol/vol, BASF) with 10 wt% fluoroethylene carbonate (FEC, Sigma Aldrich) was used as the electrolyte for half-cell measurements. Cyclic voltammetry of the cells was carried out using a galvanostat–potentiostat (VMP-3, Biologic) between 0.05 and 3.0 V versus Li+/Li at a scanning rate of 0.1 mV s^{-1} for 10 cycles and also at different scan rates. Impedance measurements were performed using a Biologic VMP-3 with a frequency range of 1 MHz to 0.1 Hz and a voltage amplitude of 10 mV. EC-Lab Z-Fit software was used to model the acquired spectra. Using the galvanostatic charge/discharge mode (Arbin), the electrochemical properties of the Fe_2O_3 anodes were measured within a voltage range of 0.05–3 V by a potentiostat.

The cyclabilities of the electrodes were evaluated at 4000 or 7000 mA g^{-1} (normalized to active mass) after 5 initial formation cycles at 100 mA g^{-1}. For rate capacity measurements, there were 6 cycles at 100 mA g^{-1}, followed by 10 cycles at various higher current rates and cycled back to 100 mA g^{-1} for 5 cycles to check the cells capacity at the end. In the extended activation process, cells were first cycled at 100 mA g^{-1} for 5 cycles followed by 30 cycles at higher currents (4000 mA g^{-1} or 7000 mA g^{-1}) and this step isrepeated 5 times. After this extended activation, rate performance at various current rates for 10 cycles is measured. The cells remained in continued cycling at 4000 mA g^{-1} (or 7000 mA g^{-1}) for further 100 cycles to check the stability of the activated electrode and finally were set back to 100 mA g^{-1} for 5 cycles to check the capacity of the cells at the end. The Coulomb efficiency was calculated from the ratio of charge capacity to discharge capacity. All specific capacities and currents were normalized to active material mass (M_{act}). The specific capacitance was calculated from the area under the CV curves[41,42] using:

$$C/M_{Act} = \frac{\int_{V_0}^{V_0+\Delta V} idV}{M_{Act}\Delta V \nu} \quad (1)$$

In practice, the integral was taken separately over positive and negatives currents and is averaged.

3. Results and Discussion

3.1. Interfacial Synthesis of α-Fe_2O_3 Flowers at an Aqueous/Organic Interface (IG-Fe_2O_3)

Although the ITIES has been exploited for nanomaterial synthesis through self-assembly or electro-synthetic routes[43–45] the interfacial synthesis of iron oxide has not been reported. Figure 1A illustrates the interfacial synthesis of iron oxide platelets at a polarized aqueous 1,2-dichloroethane (DCE) interface (see the Experimental Section for details). The compositions of the two liquid phases are given in Figure 1A, with lithium perchlorate ($LiClO_4$) and tetrabutylammonium perchlorate ($TBAClO_4$) as the supporting electrolytes in the aqueous and DCE phases, respectively. An electrodeless polarization of the ITIES is achieved through distribution of perchlorate anions (ClO_4^-) between the phases, inducing a Galvani potential difference ($\Delta_o^w\phi$) across the interface is negative of the open circuit potential (OCP) according to the Nernst–Donnan equation (Figure S1, Supporting Information).[46] As ClO_4^- is relatively hydrophobic (by comparison with Cl^- or SO_4^{2-} anions for example), it will facilitate the transfer of reactants from the organic phase, that is, 4-aminopyridine, to the aqueous phase and contribute to a higher driving force for reaction between Fe^{2+} and 4-aminopyridine. The latter induces nucleation and growth processes, leading to the self-assembly of individual flakes and particles at the interface to form 2D-structures spontaneously (Figure 1B). Furthermore, the low negative potential at the L/L interface may actually slow down the kinetics of Fe^{2+} interacting with the 4-aminopyridine at the interface. This may be the reason for the flowers forming under the conditions where Fe^{2+} is kinetically slow at reaching the interface. The effect of a polarized (with ClO_4^- ions distributed between the phases) or non-polarized (no ClO_4^- ions present) L/L interface on the morphology of the iron oxide material formed is outlined in Figure S2, Supporting Information. TBA^+ cations are also proposed to act as a structure directing reagent to take control over the morphology to lead a transition from 2D to 3D flower-like architectures (Figure S2, Supporting Information).[23] The material extracted from the interface was annealed (see Experimental Section) to improve crystallinity and remove impurities yielding a red powder as shown in Figure 1C, referred as an interfacially-grown iron oxide (IG-Fe_2O_3).

Scanning electron microscopy (SEM) of IG-Fe_2O_3 revealed a 3D-flower-like morphology, with flower sizes in the range of 4–7 µm (Figure 1D). Each 3D-flower was composed of randomly assembled, micron-sized 2D-petals. It is worth noting that the sample morphology was not visually changed by annealing (Figure S3, Supporting Information). XRD was used to examine the crystal structure of the annealed IG-Fe_2O_3 (Figure 1E). The acquired diffraction peaks were indexed to the rhombohedral structure of α-Fe_2O_3 (JCPDS 33–0664)[32] with the lattice parameters of a = 5.036 Å and c = 13.748 Å, and the space group $R3c$. No other impurities were detected, indicating the pure and single phase of α-Fe_2O_3. In addition, the intense and sharp diffraction peaks represent a high degree of crystallinity, in marked contrast to the XRD pattern obtained prior to annealing (Figure S3, Supporting Information).

Raman and infrared spectroscopies were performed to further investigate the structure of α-Fe_2O_3. Figure 1F shows the measured Raman spectrum, which contains all the expected peaks for α-Fe_2O_3: the peaks at 224 and 498 cm^{-1} are associated with A_{1g} modes while the peaks at 244, 292, 412, and 608 cm^{-1} are related to E_g modes.[32,47] The intense peak at ≈1310 cm^{-1} is ascribed to two-magnon scattering, and is consistent with previous results for nanostructured α-Fe_2O_3.[47,48] Figure 1G shows the FTIR of IG-Fe_2O_3 with distinct peaks near 520 and 433 cm^{-1} that are assigned to A_{2u}/E_u and E_u vibrational modes, respectively, which are related to the transverse stretching vibrations of Fe—O.[47]

3.2. Production and Characterization of α-Fe_2O_3 Quasi-2D Platelets

We converted the IG-Fe_2O_3 to quasi-2D nanosheets by probe-sonicating the powder in N-methyl-pyrrolidone (NMP) solvent (see Experimental Section for details). This process is similar to that used in liquid phase exfoliation (LPE)[49–51] but here it is simply being used to break up the flowers into 2D platelets. After sonication, the resultant liquid was subjected to a two-step centrifugation process,[52] expected to remove both the smallest nanoparticles and any large unfragmented material. The resultant nanosheets were transferred to isopropanol (IPA), giving a red colloidal dispersion (referred as standard dispersion as shown in **Figure 2**A) with a concentration of up to 3–4 g L^{-1}. The concentration was measured by filtering the dispersion onto a membrane and carefully weighing the deposited mass.

The most basic characterization of such dispersions is via optical extinction spectroscopy (A.K.A. UV–vis spectroscopy). The measured extinction coefficient spectrum is shown in Figure 2B and is quite broad and does not show the optical edge expected for a semiconducting material. However, for dispersions of 2D particles, extinction coefficient spectra are significantly affected by the presence of light scattering.[53,54] In fact the extinction coefficient contain contributions from both absorbance and scattering, such that $\varepsilon = \alpha + \sigma$, where α and σ are the absorption and scattering coefficients, respectively.[53,54] By using integrating sphere measurements, we separated out the contributions of α and σ, plotting them in Figure 2B alongside the extinction coefficient spectrum. This graph shows considerable scattering across the entire visible region. The absorption coefficient spectrum is as expected for a semiconductor with an absorption edge at ≈580 nm. Tauc analysis was used to estimate that the optical band gap is to be 2.2 eV (Figure S4, Supporting Information). The transition at 430 nm is attributed to overlapped contributions from ligand field transitions and the charge-transfer band tail, while the transition at 485–550 nm is the result of the pair excitation processes and are characteristics of iron oxide nanostructures.[55] It is a generally believed that 2D platelets display confinement effects, resulting in a widening of the optical gap compared to bulk materials. The obtained optical band gap for Fe_2O_3 2D dispersions are very similar to those previously reported for Fe_2O_3 nanosheets (2.2 eV) and can be compared to values of 1.8 eV for bulk Fe_2O_3.[47,55]

Transmission electron microscopy (TEM) measurements (see below for more detail) showed the contents of the dispersion to be quasi-2D platelets (inset in Figure 2C). To confirm the elemental composition of the platelets, EDX spectra were acquired on individual platelets, with each spectrum (Figure 2C) clearly showing the peaks for Fe and O (as well as C and Cu from the grid).

Next, a thin film was formed by vacuum filtration of the Fe_2O_3 standard dispersion (Figure 2D inset). An SEM image of the film surface revealed a porous network of thin 2D platelets (Figure 2D) with no non-2D material observed. Both FT-IR (Figure 2E) and Raman (Figure 2F) measurements made on this film yielded spectra which are very similar to those observed for the as-produced flowers. Figure 2G shows the XRD spectrum obtained from the 2D-platelets of α-Fe_2O_3 with that of the flowers reproduced for comparison. As with the flowers, the spectrum matched well with the rhombohedral crystal lattice structure of α-Fe_2O_3, space group R3-c (JCPDS 00-33-0664).[32] The well-defined, high intensity peaks confirmed that the platelets are highly crystalline, and the crystal structure is preserved after the exfoliation. The peak widths are virtually indistinguishable between flowers and platelets indicating that the sonication-induced fragmentation did not result in thinning of the 2D structures.

We have further characterized the 2D-platelets by high-resolution TEM and STEM imaging as well as atomic force microscopy (AFM). As shown in **Figure 3**A, the low-magnification bright-field TEM image indicates that the lateral dimension of the platelets to be 50–100 nm. To find the mean value of lateral dimension, individual platelet dimensions were measured, and statistical analysis performed. The mean platelet length and width were $\langle L \rangle = 186 \pm 5$ and $\langle W \rangle = 128 \pm 3$ nm (Figure S5, Supporting Information). Selected area electron diffraction (SAED) from a platelet oriented in [0001] direction showed a spot pattern as shown in Figure 3B indicating the single crystalline nature of the individual platelet. To examine the crystallography of the exfoliated Fe_2O_3 platelets, multiple HAADF-STEM images were acquired and averaged through rigid and non-rigid registration, as implemented in the SmartAlign code. The averaged image is shown in Figure 3C showing the hexagonal arrangement of Fe atoms, which matches with the [0001]-projected bulk structure of Fe_2O_3, as marked by a blue region in Figure 3C.

To obtain further insights into the dimensions of the platelets, we have acquired AFM images and performed statistical analysis. Figure 3D shows an AFM image of 2D-platelets of Fe_2O_3. Each platelet was individually measured using Gwydion software, to measure the length (L), width (W) and thickness (t). A total of 510 platelets were counted with the data was then plotted as in Figure 3E–G and in Figure S6A,B, Supporting Information.

Statistical analysis revealed $\langle L \rangle$, $\langle W \rangle$ and $\langle t \rangle$ are 196 ± 0.2, 139 ± 0.2 and 36±0.1 nm, respectively. The values of $\langle L \rangle$ and $\langle W \rangle$ matches well with the observed values obtained from TEM, but are slightly higher because of AFM tip-dilation effects. Taken together, the data in Figures 3E to 3G show the Fe_2O_3 flakes produced after sonication are found to be quasi-2D because their length can be considerably larger than their thickness. Figure 3E represents a scatter plot of L versus t. Clearly, $L > t$ as shown by the deviation of the data from line representing the equation, $L = t$, confirming the quasi-2D nature of these platelets. To investigate this in more detail, we calculated the aspect ratio (L/t) for each platelet, plotting the data as a histogram in Figure 3F. This histogram shows aspect ratios varying from 2 to 20 with a peak at ≈5 and a mean at $\langle L/t \rangle = 6.5$. We note that these aspect ratios are low compared to nanosheets prepared by the exfoliation of layered compounds.[56] However, as mentioned above, such low aspect ratios may be advantageous for battery materials.[21] Further, Figure 3G showed the plot of the aspect ratio (L/t) of each measured platelet versus thickness. Interestingly, this data shows a scaling of aspect ratio with thickness such that the thinnest platelets have the highest aspect ratio. Interestingly, such a trend has been seen before for

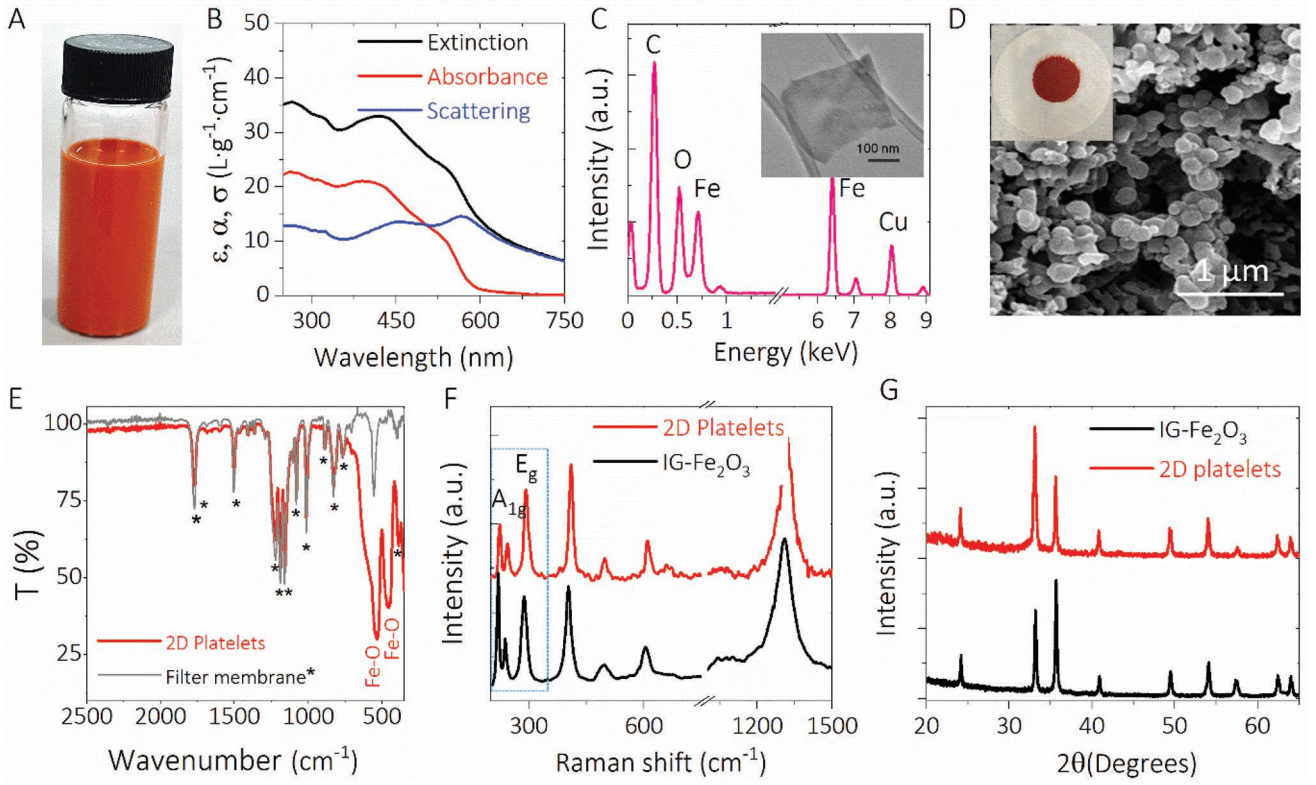

Figure 2. Liquid processing of interfacial grown α-Fe_2O_3 into quasi-2D platelets. A) Photograph of the standard α-Fe_2O_3 dispersion in IPA with a concentration of 3.8 g L^{-1}. The concentration of the dispersion was measured by filtering the dispersion onto a membrane. B) UV–visible extinction (ε), absorption (α), and scattering (σ) coefficient spectra of the standard dispersion. C) EDX spectra on individual platelet (as shown in the inset) confirming the presence of Fe and O elements. The C and Cu contributions have come from the grid. D) SEM image of the nanoplatelets. Inset: photo of a filtered film of nanoplatelets. E) FT-IR spectra of fragmented Fe_2O_3 2D-platelets were similar to that of Fe_2O_3 flower. Spectra displaying all the significant expected peaks for α-Fe_2O_3. F) A comparison of the Raman spectra of interfacial grown (IG-Fe_2O_3) and 2D platelets. Highlighted the intensity variation in the Raman modes at 223 (A_g) and 293 cm^{-1} (E_g). G) A comparison of the XRD pattern of interfacial grown (IG-Fe_2O_3) and 2D platelets. No shift in the XRD peak position of 2D platelets is observed as compared to IG-Fe_2O_3, as well as no other secondary peaks, demonstrating the pure phase of 2D platelets.

the liquid-exfoliated non-layered compound, FeF_3,[57] although its origin is unknown.

3.3. Application As an Anode in Li-Ion Batteries

As mentioned in the introduction, we have repeatedly found that 2D-materials can be fabricated into lithium ion battery electrodes with the highest achievable capacity once single-walled carbon nanotubes (SWNT) are used in place of both conductive additive and polymeric binder.[19,20,35,40] Here, for electrode fabrication, the dispersions of α-Fe_2O_3 nanosheets were mixed with CNTs (mass fraction 28–30%) and vacuum filtered onto a separator to give films with a thickness of ≈6 µm (Figure S7A, Supporting Information). Top-view and cross-sectional SEM images on such films (**Figure 4**A,B) indicate that the Fe_2O_3 flakes are uniformly embedded in a well-dispersed CNT network. Such electrodes are enhanced by the highly conductive and mechanically tough CNT network which facilitates charge distribution while ensuring mechanical integrity even during charge/discharge induced expansion. These composites also incorporate an extensive pore network which allows for efficient liquid-phase diffusion of Li ions within the electrode. This combination results in the maximization of capacity, rate capability, and cyclability.[20,38,58]

We performed preliminary electrochemical characterization on these composite electrodes via cyclic voltammetry (CV) measurements. Figure 4C presents CV curves measured on a fresh (no activation) Fe_2O_3/CNT electrode in the potential range of 0.05–3.0 V (versus Li^+/Li), measured at a scan rate of 0.1 mV s^{-1}. In the first cycle, three cathodic peaks (1c, 2c, and 3c) were observed at 1.56, 0.94, and 0.65 V, respectively, corresponding to the following multistep reduction processes.[34,59]

$$\alpha - Fe_2O_3 + xLi^+ + xe^- \rightarrow \alpha - Li_xFe_2O_3 \quad (2)$$

$$\alpha - Li_xFe_2O_3 + (2-x)Li^+ + (2-x)e^- \rightarrow Li_2Fe_2O_3 \quad (3)$$

$$Li_2Fe_2O_3 + 4Li^+ + 4e^- \leftrightarrow 2Fe^0 + 3Li_2O \quad (4)$$

Thus, the overall reversible reaction can be simply summarized as

$$Fe_2O_3 + 6Li^+ + 6e^- \leftrightarrow 2Fe + 3Li_2O \quad (5)$$

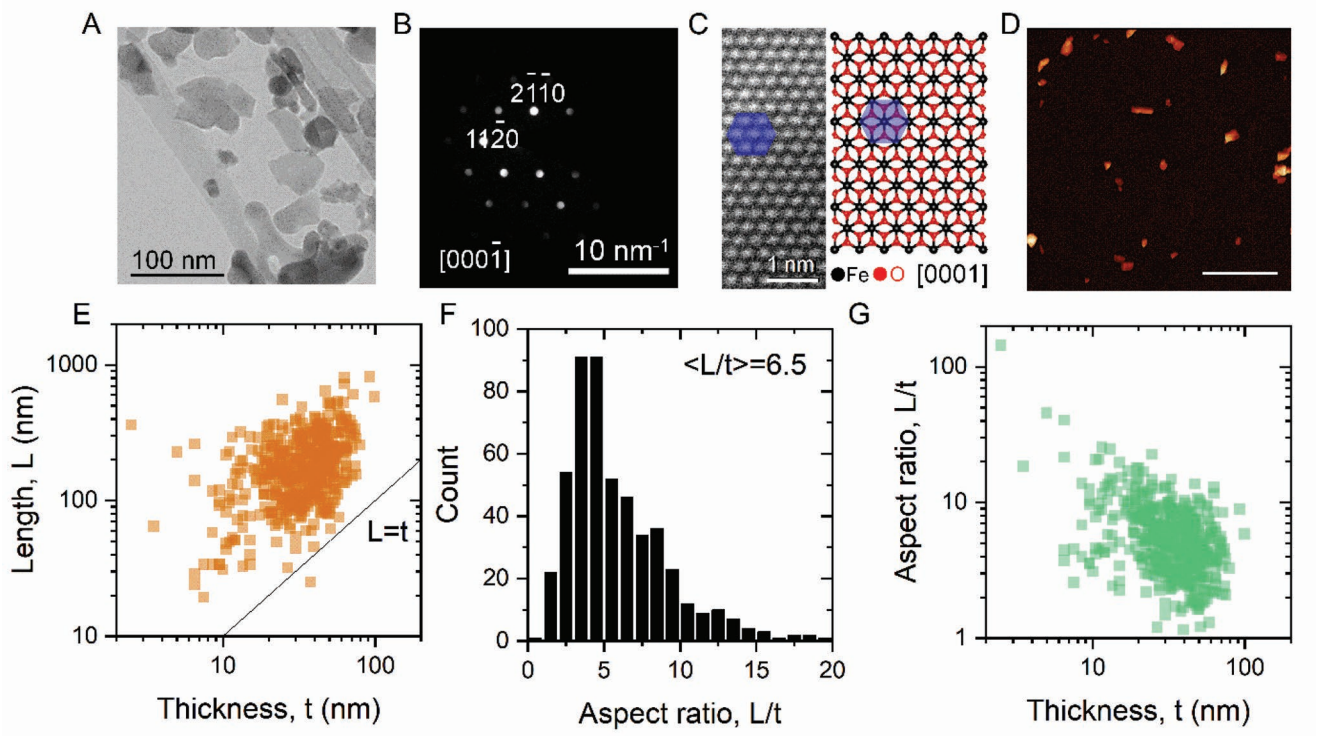

Figure 3. Size and thickness analysis of 2D platelets from the standard α-Fe_2O_3 dispersion. A) Low magnification bright-field TEM image of Fe_2O_3 confirming 2D-platelets like morphology. B) Selected area electron diffraction pattern from an individual flake. The diffraction spots were assigned to the Miller index $11\bar{2}0$ and $2\bar{1}\,\bar{1}0$ corresponds to the atomic planes of rhombohedral crystal lattice structure of α-Fe_2O_3. C) HAADF-STEM image from the flake showed the hexagonal arrangement of Fe atoms, which matches with the [000$\bar{1}$] crystallographic projected bulk structure of Fe_2O_3. The Fe and O atoms are shown in black and red, respectively. D) AFM image of liquid exfoliated 2D-platelets. E) Length versus thickness scatter plot. Each point on the plot represents the dimension of an individual platelet measured by AFM. F) Histogram showing distribution of aspect ratios for the platelets in the standard dispersion. G) Plot of aspect ratio (L/t) of each individual platelet versus thickness.

In the first cycle, the small reduction peak at 1.56 V (1c) is attributed to Li insertion into α-Fe_2O_3, without any structural transition (Equation (2)) (this defines the intercalation region of 3.0–1.5 V). The second reduction peak at 0.94 V (2c) is assigned to the phase transition from hexagonal α-$Li_xFe_2O_3$ to cubic Li_2Fe_2O (Equation (3)) (defines the phase transition region of 1.5–1.0 V). This reaction is irreversible and is not observed in subsequent cycles. The more prominent peak centered at 0.65 V (3c) corresponds to the complete reduction of Fe^{3+} to Fe^0 which is accompanied with the formation of Li_2O (Equation (4)) (this defines the main conversion region of 1.0–0.5 V).[12,22]

In addition, two broad anodic peaks appear at 1.66 and 1.88 V which correspond to the reversible oxidation of Fe^0 to Fe^{2+} and further oxidation to Fe^{3+}, results which are consistent with previous reports.[12,23,32,34] The overall reversible conversion reaction can be simply summarized by Equation (6), which indicates the storage of 6 mol of Li^+ per formula unit, consistent with a theoretical capacity of 1007 mAh g^{-1}.[60] In the subsequent cycles, both cathodic and anodic peaks are slightly shifted owing to structural modifications and yielding the new reduction peak at 0.81 V. The notable overlapping of the CV curves from the second cycle onward implies the good reversibility and stability of the electrochemical reaction.

Next, we performed galvanostatic charge–discharge experiments on a Fe_2O_3/CNT electrode. It is of specific relevance that this electrode was first activated via five 100 mA g^{-1} charge/discharge cycles. This is a reasonably standard activation procedure which allows the solid electrolyte interface (SEI) layer to form. After the activation cycles, we performed 195 charge–discharge cycles at the higher current of 4000 mA g^{-1}. The voltage profiles associated with the 1, 6, 100, and 200 cycles are shown in Figure 4D (voltage range 0.05–3.00). During the lithiation process, three plateau regions are observed (Figure 4D) in the voltage ranges from 1.7 to 1.50 V, 1.25 to 1.00 V and 1.0 to 0.50 V, respectively. The plateau regions correspond to the three processes described by Equations (2)–(4) and show reasonable agreement with the peaks observed in the CV curves (Figure 4C and Figure S7B,C, Supporting Information). After the first five activation cycles, the GCD profiles show good overlap indicating excellent reversibility of the lithium storage reaction.

Figure 4E shows the charge and discharge capacities for both the first five activation cycles and the subsequent measurement cycles. Unless otherwise stated, all capacities are normalized to active mass. During the first activation cycle at 100 mA g^{-1}, the Fe_2O_3/CNT electrodes deliver a very high initial discharge and charge capacity of 2206 and 1584 mAh g^{-1} (Figure 4E), respectively. This difference is mainly attributed to the electrolyte decomposition during the formation of the solid electrolyte interface (SEI) as well as structural pulverization and entrapment of some lithium in the active material.[61] This apparent

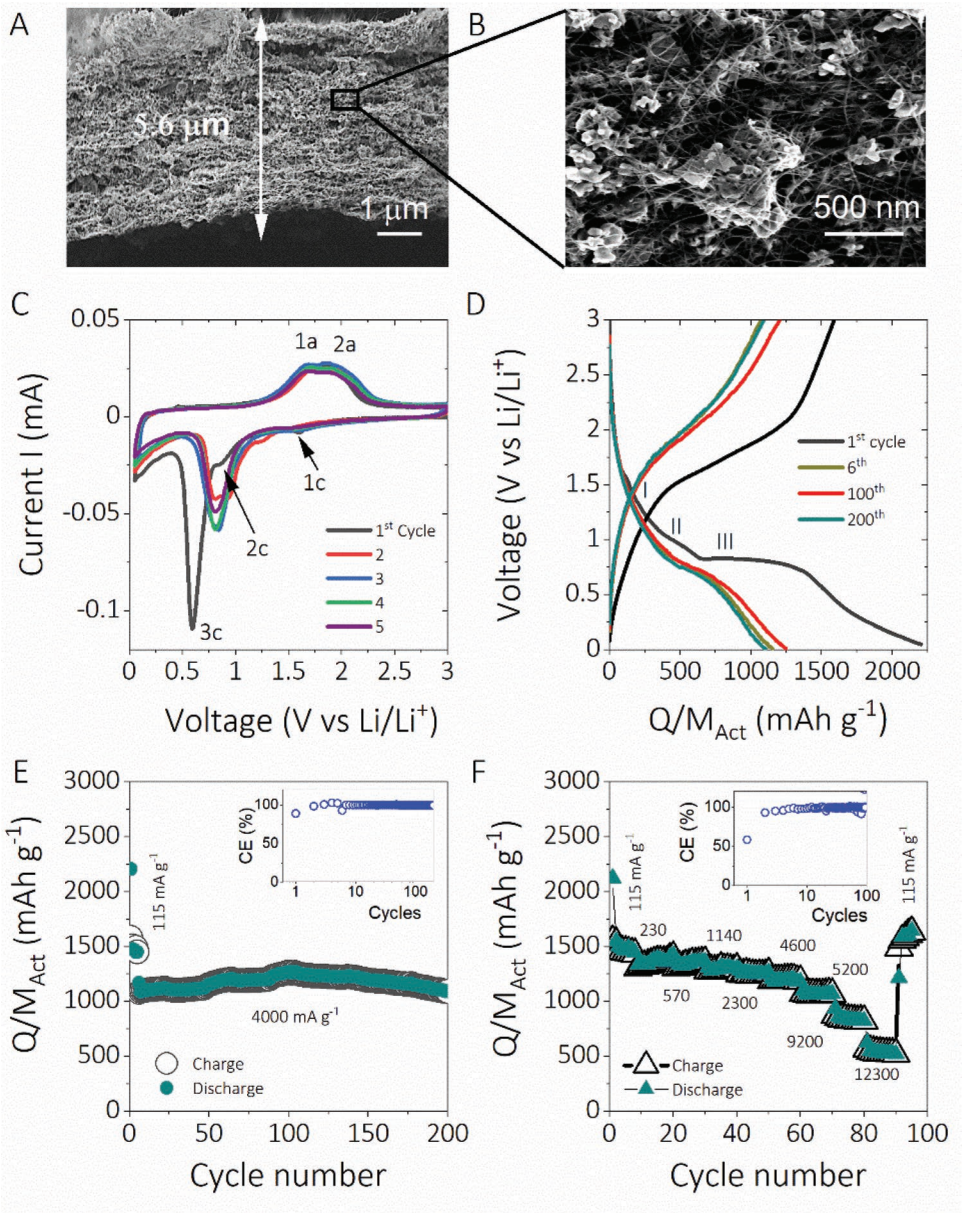

Figure 4. Electrochemical performance of α-Fe_2O_3 nanoplatelet/CNT composites as lithium-ion battery anodes (M_f^{CNTs} = 30%, A = 0.178 cm^2, M_T/A = 0.67 mg cm^{-2}). A,B) SEM images of α-Fe_2O_3/CNT composite film at two magnifications. Approximate α-Fe_2O_3/CNT composite electrode thickness was 5.9 µm. C) The first five consecutive CV curves of α-Fe_2O_3/CNT composite at a sweep rate of 0.1 mV s^{-1}. D) Galvanostatic charge–discharge voltage profiles of α-Fe_2O_3/CNT composite electrodes for 1, 6, 100, and 200 cycles. E) Both charge and discharge cycling capacity for the α-Fe_2O_3/CNT composite anodes cycled at 100 mA g^{-1} for first five cycles and 4000 mA g^{-1} for 200 cycles. Inset shows the Coulombic efficiency as a function of cycle number. F) Rate capability of α-Fe_2O_3/CNT composite electrode as a function of cycle number at various specific currents from 115 to 12 300 mA g^{-1}. Inset shows the Coulombic efficiency as a function of cycle number. All specific capacities and currents are normalized to the mass of the active material Fe_2O_3.

capacity difference and the resultant low initial Coulomb efficiency (inset Figure 4E) is a very common feature in nanostructured electrodes.[22] Over the next four activation cycles, the reversible discharge capacity gradually decreased from 1486 to 1450 mAh g^{-1} while the Coulombic efficiency rose to 100%. After the fifth activation cycle, the current was increased to 4000 mA g^{-1}, with the discharge capacity dropping to 1160 mAh g^{-1} (for the 6th cycle) as expected due to the rate increase. The capacity was quite stable, displaying 1260 mAh g^{-1} for the 100th cycle and 1100 mAh g^{-1} for the 200th cycle (Figure S7, Supporting Information, for dQ/dV profiles for 6, 100 and 200 cycles, no obvious change was noticed). We note that, because the specific capacity of the nanotubes used here is low (<100 mAh g^{-1}), we don't expect them to contribute to the measured capacity in any significant way.[58]

Rate performance measurements were also performed on Fe_2O_3/CNT electrodes as shown in Figure 4F. We found an average discharge capacity of 1445 mAh g^{-1} when measured

using a current density of 115 mA g^{-1}. As the current was increased, the measured capacity fell off, reaching ≈1185 and 532 mAh g^{-1} at currents of 4600 and 12 300 mA g^{-1}, respectively. Interestingly, after the 90 cycles, when the current density was returned to 115 mA g^{-1}, the capacity reached 1600 mA h g^{-1}, somewhat higher than the initial value. This slight increase in capacity suggests the electrodes experience a continual activation process during cycling leading to non-trivial capacity gains.

The capacity versus current data shown above are already very impressive compared to published literature for Fe_2O_3 (see below and Table S1, Supporting Information). To our knowledge, all but two papers report reversible capacities for Fe_2O_3 which were below 1300 mAh g^{-1}. Of the other two, the highest previously reported reversible capacity for Fe_2O_3 was ≈2000 mAh g^{-1} (after 300 cycles),[13] which is comfortably above our value of ≈1500 mAh g^{-1}. However, there is reason to believe that this value can be increased as we will describe in the next section.

3.4. Achieving Very High-Capacity Electrodes via Extended Activation

In discussing the rate performance above, we noted an apparent gradual increase in capacity with cycling. This suggests that performing an extended activation process, which goes beyond the standard five cycles used above, might yield electrodes with a capacity higher than that observed in Figure 4. In this section, we will explore such an extended activation process. However, to activate at 100 mA g^{-1} for many cycles would require a prohibitively long time. To avoid this, we initially, attempted activation at relatively high currents, 4000 and 7000 mA g^{-1} over many cycles. However, preliminary tests showed that, although the measured capacity didn't change appreciably with cycle number, if a rate performance test was performed after such high-current cycling, increased capacities were observed at low current.

This prompted us to develop an innovative procedure where we activated the electrode by repeated cycling at high current (either 4000 mA g^{-1} as shown in **Figure 5**A, or 7000 mA g^{-1} as shown in Figure S8, Supporting Information). However, every 30 cycles (including at the start of the experiment), we applied a "probe" where we cycled for 5 cycles at low current (100 mA g^{-1}). The idea was that these probe cycles would tell us whether the low-current capacity was increasing in response to the high-current activation. Assuming we did see an increase in low-current capacity, we then applied a rate-performance measurement (to allow analysis of the activated electrode) followed by continued cycling at high current to see if the activated electrode was stable. A more detailed description is given in the Supporting Information.

The results of such an experiment using 4000 mA g^{-1} activation are shown in Figure 5A. The initial 100 mA g^{-1} probe cycles (1 to 5) showed a charge capacity of roughly 1535 mAh g^{-1} consistent with Figure 4F. The subsequent 4000 mA g^{-1} cycles (up to cycle 125) showed a constant discharge capacity at roughly 1012 mAh g^{-1}, again consistent with Figure 4F. However, the 100 mA g^{-1} probe cycles (31–35, 61–65, 91–95, 121–125) showed a successive increase in capacity, exceeding 2000 mAh g^{-1} by cycle 125. These results reveal that our extended activation at high current (4000 mA g^{-1}) yield a significant capacity increase at low current (100 mA g^{-1}) that is not visible during the 4000 mA g^{-1} cycling.

After this activation process, we performed a rate performance test. We continued cycling at 100 mA g^{-1} until 145 cycles after which we applied increasing currents, each for a 5 cycles duration before ending this phase of the experiment at 16 000 mA g^{-1} after 229 cycles (Figure 5A). We found the expected fall off in capacity with increasing current, although the capacity decay appeared to be more severe than that observed in Figure 4F for the normally activated sample. We will perform a quantitative rate-performance analysis later. After the 16 000 mA g^{-1} current, we reverted to 100 mA g^{-1} (230–234 cycles) and found the discharge capacity returned to its post-activation, low-current level of 2100 mAh g^{-1}.

After the rate performance, we performed continued cycling at constant current (4000 mA g^{-1}, 235–334 cycles) to test the electrode stability post-cycling. After a slow rise over ≈35 cycles, the discharge capacity saturated at ≈1000 mAh g^{-1}, very close to its previous value when both cycled and measured at 4000 mA g^{-1}. We completed the experiment by reducing the current to 100 mA g^{-1} (335–344 cycles), finding the discharge capacity to return to 2115 mAh g^{-1}. Taken together, the data set in Figure 5A shows that the low-rate capacity can be increased significantly but extended cycling at high current and that the resultant discharge capacity is relatively stable up to at least 350 cycles. Similar results were found when activating at 7000 mA g^{-1} (see Figure S8, Supporting Information). Moreover, Fe_2O_3 quasi 2D-platelets/CNT composite electrodes display significantly high performance as compared to IG-Fe_2O_3 flowers/CNT composite electrodes (see Figure S9, Supporting Information).

In order to elucidate the effect of the extended activation process, a number of characterization procedures were performed comparing identical Fe_2O_3/CNT electrodes before and after extended activation. When SEM cross section images of the Fe_2O_3/CNT composite electrode are examined before (Figure 5B) and after activation (Figure 5C), the most obvious difference is a thickness increase from 5.9 μm before activation to 8.8 μm afterward. Considering the electrode mass as well as the densities of Fe_2O_3 and CNT and the CNT mass fraction, this expansion implies an increase in electrode porosity from 79% to 85%. We note that the electrodes before activation were extremely porous, considerably higher than values of ≈50–60% found for previous nanosheet/nanotube composites.[39] These SEM images clearly show a morphological change after cycling. While Figure 5B shows well-defined particles embedded in a nanotube network, the texture of the post-cycling electrode in Figure 5C appears different. Although nanotubes are still visible, well-defined particles are no longer clearly seen. We can confirm that the chemical compositional change has not occurred with EDX showing the electrode to consist of carbon, iron, and oxygen in similar proportions as before (Figure S10, Supporting Information).

One might speculate that the textural changes revealed by the SEM images might indicate a transformation of the crystalline Fe_2O_3 into fully amorphous material during activation. To test this, we performed XRD on electrodes both before and

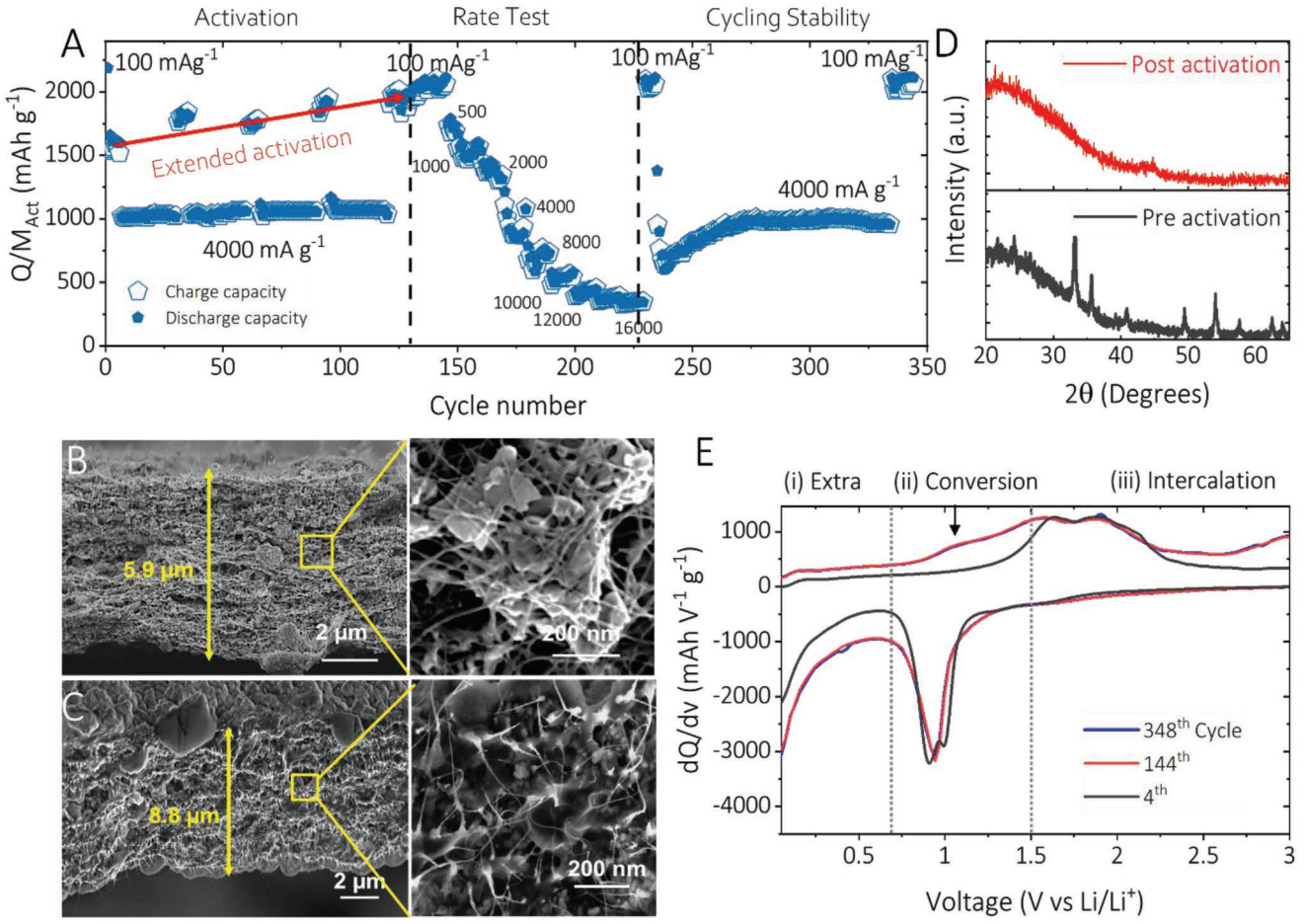

Figure 5. Effect of an extended activation on the performance of α-Fe_2O_3/CNT composite electrode ($M_f^{CNTs} = 30\%$, $A = 0.178$ cm^2, $M_T/A = 0.67$ mg cm^{-2}). A) Galvanostatic charge–discharge cycling performance of the α-Fe_2O_3/CNT composite electrode with an extended activation processes at two different current densities 100 (for 5 cycles) and 4000 mA g^{-1} (30 cycles) with four repetitive times. In all cases, capacity and currents are normalized to the active mass of the α-Fe_2O_3. B) SEM images of the α-Fe_2O_3/CNT composite electrode before and C) after the extended activation processes of 145 cycles. D) X-ray diffraction pattern of α-Fe_2O_3/CNT composite anodes before and after the extended activation processes. E) dQ/dV versus voltage curves for 4th, 144th, and 348th cycles at 100 mA g^{-1}.

after activation (Figure 5D). The crystalline nature of the pre-cycling electrode can clearly be seen via the various diffraction peaks. However, after cycling no peaks are visible, which proves that the film is fully amorphous.[14,62] This is consistent with literature reports showing both the alloy and conversion type materials undergo amorphization processes upon prolonged cycling leading to the formation of amorphous materials, and pulverization induced particle size reductions.[12,62–64]

The data in Figure 5B–D shows that extended activation increases the porosity and leads to an amorphization of the Fe_2O_3. To further examine how these changes lead to extra capacity, we examine the voltage profiles, first converting them to dQ/dV versus voltage graphs. Figure 5E displays dQ/dV versus V plots during the selected cycles at 4 (during the first set of probe cycles, before activation), 144 (after activation, before rate measurement), and 348th (after activation, after final stability cycling) at a current density of 100 mA g^{-1} (see Figure S11, Supporting Information) for comparison of different cycles when the current density switches back to a low rate (100 mA g^{-1}). The first and most obvious difference between the curves collected at different cycle numbers is that the 144 and 348 cycle curves are virtually identical to each other but are significantly different to the cycle 4 curve. This indicates that the activation process is complete after 144 cycles and the material is electrochemically stable thereafter.

To perform further analysis we note that the potential range of these graphs (Figure 5E) can be divided into three regions which have previously been associated with:[12] i) the intercalation region where Li^+ intercalates into α-Fe_2O_3 (3.0–1.5 V); ii) the main conversion region where the reduction of α-Fe_2O_3 into Fe^0 takes place (1.5–0.6 V); iii) a region of extra capacity (0.6–0.001 V), where the reversible electrolyte decomposition occurs. As it can be seen in Figure 5E, in the cathodic region, the effect of activation, as manifested by the differences between cycle 4 and 144 is concentrated in region (i) between 0.6 and 0.001 V. These changes are associated with reversible electrolyte decomposition[12] which is logically connected with the internal surface area of the electrode. This implies that the capacity increase after cycling is linked to an increase in the internal surface area, which must be connected to the

morphology changes described above.[12,63,65] The combination of increased internal surface area and increased porosity implies the generation of new pores during activation. This is consistent with literature reports showing that the lithiation-induced nanopore formation can take place on metal, metal oxides, and semiconductor nanocrystals/nanowires upon lithiation/delithiation cycles.[64,66,67]

In addition, we notice some peak shifts in the dQ/dV curves after activation. For the 4th cycle (before activation), the voltage hysteresis between the conversion (0.9 V) and deconversion (1.63 V) peaks is 0.73 V. After extended activation, the conversion peak has shifted slightly to 0.94 V while the deconversion peak has moved to 1.58 V. In addition, a second apparent deconversion peak has appeared at 1.07 V. After activation, the voltage hysteresis between conversion and deconversion peaks is reduced to 0.64 V. The values of voltage hysteresis both before and after activation are significantly smaller than the value of ≈1 V usually reported in the literature.[60,68] That the pre-activation voltage hysteresis in our electrodes is <1 V may be due to the porous nature of our electrode which may enable efficient conversion of Fe_2O_3 particles to Li_2O and Fe, as well as deconversion back to the intercalated phase without creating a large density of Li_2O/Fe interfaces (minimizes the Li_2O/Fe interface density generation during the conversion reaction).[69] If this is correct, then the further reduction in voltage hysteresis after activation may be due to the further increase in porosity.

3.5. Quantitative Analysis of Rate Performance Before and After Activation

It is possible to gain further insights into the effects of activation via quantitative analysis of the rate performance of the electrodes. We start by examining the dependence of cyclic voltammetry on voltage scan rate, ν, before (on fresh electrode) and after extended activation processes (**Figure 6**A). Both sets of CV curves shows similar shapes with anodic peaks at ≈2 V and cathodic peaks at ≈0.7 V. Notably, the anodic peaks are slightly upshifted and both sets of peaks broadened after activation, probably due to the morphological changes during activation.[62] As the scan rate was changed from 0.1 to 1 mV s^{-1} a slight increase in the reaction overpotential was observed indicating that the polarization was small, and the electrochemical reaction kinetics improved.

The specific capacitance of the Fe_2O_3/CNT composite electrodes before and after activation was calculated for each scan rate from the area under the curve. Figure 6B presents the specific capacitance of the Fe_2O_3/CNT composite electrodes before and after activation as a function of scan rate ranging from 0.1–1 mV s^{-1}. Significantly, the activated electrode displays considerably higher capacitance at all scan rates. In the intrinsic, low-rate region, the specific capacitance is approximately three times larger after activation (see also, Figure S12, Supporting Information). All other things being equal, this implies that the internal surface area of the Fe_2O_3/CNT composite electrode is increased by ×3 after activation, consistent with the discussion above. In addition, while the capacitance before activation was roughly constant in this scan range, after activation, we find a roughly 50% decrease in capacitance as the scan rate was increased from 0.1 to 1 mV s^{-1}, indicating that activation has reduced the rate performance of the electrode.

We can assess the factors limiting the current during the CV measurements by plotting the peak current (measured at 0.79 V), i_p, versus ν in Figure 6C. Plotted on a log–log plot, these plots are straight lines consistent with, $i_p \propto \nu^b$. Generally, diffusion-limited currents display $b \approx 0.5$, whereas a capacitive-limited process yields $b \approx 1$.[70] Here we found b-values 0.81 before activation and 0.58 after activation indicating the electrode evolves from capacitive limited (before activation) to diffusion limited after extended action.

We can analyze this in more detail by assuming the cathodic current has both diffusion- and capacitance-limited components such that the peak current is given by:

$$i_p = k_C \nu + k_D \nu^{1/2} \tag{6}$$

with the subscripts indicating the capacitive and diffusive components.[70] We plot the data as $i_p/\nu^{1/2}$ versus $\nu^{1/2}$ in Figure 6D. We find good linearity demonstrating the validity of Equation (6) with fitting yielding values of k_C and k_D as shown in the figure. Using these parameters, we plot the ratio of capacitive to diffusive current components in the inset of Figure 6D. This plot confirms that while the capacitive limited current is dominant before activation at most (i.e., higher) scan rates, the diffusion limited current becomes dominant after activation.

The Randles–Sevcik equation predicts that the peak current observed in a CV experiment scales with electrode area and ion diffusion coefficient as $i_p \propto AD^{1/2}\nu^{1/2}$. Although, it is tempting to use this equation, to fit the rate dependent current data, this is not strictly appropriate as this equation was derived to describe diffusion in a semi-infinite bulk liquid followed by reaction at a flat planar electrode.[71] However, we can approximately use this equation by considering A as the total internal surface area of the electrode, A_{Int} (rather than the geometric area), and D as the diffusion coefficient of ions in the electrode pores, D_{Pore} (rather than in bulk liquid, D_{BL}). The diffusion coefficient in the pores is reduced relative to that in bulk liquid as described by the Bruggeman equation: $D_{Pore} = D_{BL}P/\kappa$, where P is the porosity of the electrode and κ is the tortuosity factor.[72,73] Then, if we associate the Randles–Sevcik equation with the second term in Equation (6), we can write:

$$\frac{k_{D,After}}{k_{D,Before}} = \frac{A_{Int,After}}{A_{Int,Before}} \left(\frac{P_{After}}{P_{Before}} \frac{\kappa_{Before}}{\kappa_{After}} \right)^{1/2} \tag{7}$$

Because we know the values of k_D and P both before and after activation (above) and the capacitance data implies that $A_{Int,After}/A_{Int,Before} \approx 3$, this allows us to estimate that $\kappa_{After}/\kappa_{Before} \approx 0.75$. This indicates that activation has reduced the pore tortuosity of the electrode slightly. This is understandable as electrodes consisting of platelets are expected to have high tortuosity[21] and implies that morphology change associated with the amorphization leads to a less platelet-like geometry.

Finally, we perform quantitative analysis of the battery rate performance data for both the normally-activated electrodes (previously shown in Figure 4F) and that for the electrode following extended activation (previously shown in Figure 5A), as shown in Figure 6E. We assume that the normally activated electrode is comparable to an electrode before extended activation. Plotted on the same graph (stars) is literature data for Fe_2O_3-based electrodes

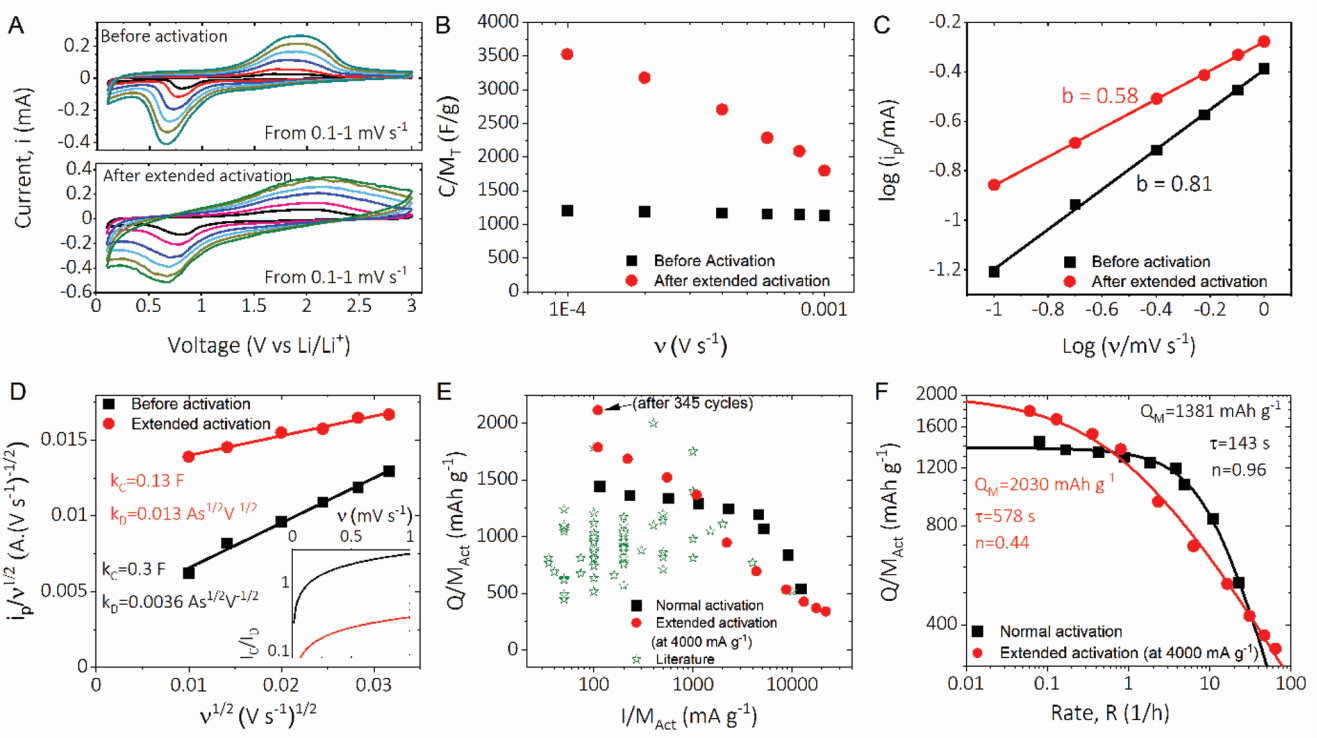

Figure 6. A) CV curves collected at various scan rates from 0.1 to 1 mV s^{-1} both before and after the extended activation processes. B) Specific capacitance of the Fe_2O_3/CNT composite electrodes before and after activation, normalized to active mass, as a function of scan rate ranging from 0.1–1 mV s^{-1}. C) Log(i_p) versus log(ν) plot of the cathodic current response (i_p measured at 0.79 V). D) Plot of $i_p/\nu^{1/2}$ versus $\nu^{1/2}$ for Fe_2O_3/CNT composite electrode before and after activation with values of the capacitive (k_C) and diffusive (k_D) components shown. Inset shows the plot of ratio of capacitive limited current and diffusion limited current, (I_C/I_D) as a function of scan rate. E) Comparison of specific capacity versus current data obtained for Fe_2O_3/CNT composite electrode in this work to previous literature data. In all cases, capacity and currents are normalized to the active mass. F) Specific capacity as a function of charging rate (defined as $R = (I/M_{Act})/(Q/M_{Act})$) for Fe_2O_3/CNT composite electrode (M_f^{CNTs} = 30%, A = 0.178 cm^2, M_T/A = 0.67 mg cm^{-2}). After activation, n = 0.44 indicating, Fe_2O_3/CNT composite electrode moves from capacitive limited to diffusive limited upon cycling. The lines are fits to Equation (8) and fit parameters are given in the inset. All specific capacities and currents are normalized to the mass of the active material Fe_2O_3.

(all data sets are collected from a subset of the papers which are listed in Table S1, Supporting Information). There are a number of things to note. First, while the extended activation process effectively improves the capacity at low rate, it yields reduced capacities at a high rate. These differences in rate performance must be caused by the morphological changes discussed above as we will show below. In addition, it is clear from this plot that the performance of 2D-Fe_2O_3-based electrodes both before and after extended activation is superior to the literature data at all rates.

To study quantitative rate analysis, in Figure 6F we plot the measured specific capacity (Q/M_{Act}) (normalized to Fe_2O_3 mass, that is, not including the CNT mass) versus the parameter, R, which is defined via $R = I/Q$, that is, the ratio of the current to the stored charge (this is of course equal to the ratio of specific current to specific capacity).[74–78] In this way, $1/R$ is a measure of the actual charge/discharge time of the electrode at constant current. This data shows the measured capacity to fall off with rate as is generally observed.[21,78] To fit this data, we use a semiempirical equation that was proposed recently by us:[78]

$$Q/M_{Act} = Q_{M,Act}\left[1-(R\tau)^n\left(1-e^{-(R\tau)^{-n}}\right)\right] \quad (8)$$

Such a fitting can yield three fit parameters: $Q_{M,\,Act}$, the capacity at very low rate which can be compared to the theoretical capacity (normalized to active mass); τ, the characteristic time associated with charge/discharge and n, a parameter similar to b whose value indicates the dominance of diffusive (n = 0.5) or electrical (n = 1) limitations on rate performance.[21,74,75,77,78] As shown in Figure 6F, this equation fits the data extremely well for both for the normally activated electrodes and those subjected to extended activation. The obtained fit values were $Q_{M,Act}$ = 1381 mAh g^{-1}, n = 0.96 and τ = 143 s for the normally activated sample and $Q_{M,Act}$ = 2030 mAh g^{-1}, n = 0.44 and τ = 578 s for the extended activation sample. We will discuss these fit parameters one by one.

First, we note that, even with normal activation the value of $Q_{M,Act}$ = 1381 mAh g^{-1} is considerably higher than the theoretical capacity of Fe_2O_3 (1007 mAh g^{-1}). However, this is consistent with previous reports on Fe_2O_3 based electrodes[10] and with certain classes of 2D material which display an anomalously-high, low-rate capacity.[21] Extended activation increases the low-rate capacity to $Q_{M,\,Act}$ = 2030 mAh g^{-1}, which is over twice the capacity of previous iron oxide electrodes. As described above, this is likely due to a surface-based Li storage mechanism with the increased capacity linked to increased surface areas. This anomalously high, surface-based capacity is reminiscent of that found in MoO_2-based electrodes.[79]

The change from n = 0.96 for the normally activated sample to n = 0.44 s for the extended activation sample is especially

interesting. As mentioned above the value of n indicates the dominance of diffusive ($n = 0.5$) or capacitive/electrical ($n = 1$) limitations on rate performance.[21,74,75,77,78] These results clearly show that while the normally activated sample is mostly limited by capacitive/electrical effects, the extended activation sample is predominately limited by diffusive effects. It is important to note that this is completely consistent with the capacitance data (and b-values) from Figure 6B–D.

Finally, we found that τ changes from 143 s for the normally activated sample and to 578 s for the extended activation sample. We can analyze τ in two ways: as a figure or merit for rate performance and as providing information on the charge/mass transport mechanisms in the electrode. First, τ is a measure of the rate (R) above which the capacity begins to fall off. As such it can be thought of as the minimum charging time required to achieve maximal capacity meaning that small values of τ are desirable.[76,78] However, it is impossible to assess rate performance properly without considering electrode thickness, simply because τ depends strongly on electrode thickness.[21,74,78] Previously, we have shown that a reasonable figure of merit for rate performance is τ/L_E^2 as this accounts for most of the thickness dependence (but not all).[21,78] For the samples under study here we found values of τ/L_E^2 to be of 4.1×10^{12} and 7.5×10^{12} s m^{-2} for the normal activation and extended activation electrodes respectively. To put this into context, Tian et al.[21] have published values of τ/L_E^2 for dozens of published materials divided into two cohorts "2D materials" and "all materials" (see their Figure 5C,D). We note that the values quoted above are actually highly-competitive in both cohorts, once the thickness of our electrodes is considered. For example, for 2D-based electrodes of thickness 5–10 µm, values of τ/L_E^2 extracted from published works lie in the range $\approx 4 \times 10^{11}$ to $\approx 10^{14}$ s m^{-2} (smaller values indicate better rate performance).[21] Our values of $4 - 8 \times 10^{12}$ s m^{-2} lie at the lower end of this range indicating that our electrodes are competitive with the best 2D materials.

In another paper, Tian et al.[78] proposed an equation relating τ to various physical properties of the electrode/separator system. This model has been validated in numerous subsequent papers.[74–77] In Table S2, Supporting Information, we combine this model with known/plausible values of these parameters, including the known diffusion coefficient of Li in crystalline Fe_2O_3 (6×10^{-12} s m^{-2}, Ref. [23]), to obtain a predicted τ-value before the activation of 120 s, in good agreement with the measured value of 143 s. Before activation, the model predicted capacitive and diffusive contributions to τ of 88 and 32 s, respectively, consistent with the prediction that the normally activated sample is capacitance limited. However, the only way the model could reproduce the observed increase in τ after extended activation was assuming a post-activation solid state diffusion coefficient of 10^{-13} cm^2 s^{-1}, a significant decrease compared to the normally activated sample. It is not clear why extended activation should result in such a slow solid-state diffusion. However, we propose it is linked to the morphological changes associated with extended activation.

4. Conclusion

In summary, we have demonstrated the production of quasi-2D Fe_2O_3 in the form of nano-flowers using an interfacial synthesis technique. By using sonication to break up these nano-flowers, we converted the as produced material into quasi-2D nanoplatelets. These nanoplatelets were identical to the nano flowers in all aspects except their shape. AFM characterization confirmed the platelets to be quasi-2D-like with, on average, a relatively low aspect ratio. However, we did note that thinner flakes had a larger aspect ratio, >10 for those flakes with a thickness below 10 nm. We fabricated lithium-ion battery anodes by combining the Fe_2O_3 nanoplatelets with carbon nanotubes. We found that such anodes performed extremely well displaying low-rate capacities approaching 1500 mAh g^{-1}, competitive with the best reported literature results. However, we also found that when subjected to an extended activation process these electrodes displayed considerably enhanced low-rate capacities of just above 2000 mAh g^{-1} (2115 mAh g^{-1} after 345 cycles). We found that the activation procedure which leads to this enhanced capacity resulted in an amorphization of the iron oxide coupled with an increase in porosity and hence internal surface area. While these morphological changes resulted in the observed increase in low-rate capacity, our results imply that they also result in a reduced Li ion solid state diffusion coefficient. This reduced ion mobility after activation has a significant negative effect on the rate performance of these electrodes. This means that Fe_2O_3/CNT composites can either be used in minimally activated form to yield electrodes with good low-rate performance and reasonable rate performance or they can be activated to increase the low-rate capacity but at the cost of reduced rate performance at higher currents.

Supporting Information

Supporting Information is available from the Wiley Online Library or from the author.

Acknowledgements

H.K. and R.T. contributed equally to this work. J.N.C. acknowledges the European Commission (Graphene Flagship Core 3, grant agreement No. 881603, respectively), the European Research Council Advanced Grant (FUTURE-PRINT), and Science Foundation Ireland (SFI,11/PI/1087). The authors have also received support from the Science Foundation Ireland (SFI) funded center AMBER (2-PF-EFM-209152) and availed of the facilities of the SFI-funded AML and ARM labs. B.K. acknowledges EDGE MSCA under grant number 713567 for research funding. M.D.S. acknowledges the European Research Council through a starting grant (agreement no. 716792).

Open access funding provided by IReL.

Conflict of Interest

The authors declare no conflict of interest.

Data Availability Statement

The data that support the findings of this study are available on request from the corresponding author. The data are not publicly available due to privacy or ethical restrictions.

Keywords

carbon nanotubes, Fe_2O_3, high capacity, liquid-liquid interfaces, lithium-ion batteries, quasi-2D platelets

Received: June 24, 2022
Revised: August 2, 2022
Published online: September 1, 2022

[1] K. Kang, Y. S. Meng, J. Breger, C. P. Grey, G. Ceder, *Science* **2006**, *311*, 977.
[2] H. Cheng, J. G. Shapter, Y. Li, G. Gao, *J. Energy Chem.* **2021**, *57*, 451.
[3] W. Qi, J. G. Shapter, Q. Wu, T. Yin, G. Gao, D. Cui, *J. Mater. Chem. A* **2017**, *5*, 19521.
[4] P. G. Bruce, B. Scrosati, J. M. Tarascon, *Angew. Chem., Int. Ed. Engl.* **2008**, *47*, 2930.
[5] N. Nitta, F. Wu, J. T. Lee, G. Yushin, *Mater. Today* **2015**, *18*, 252.
[6] S.-H. Yu, X. Feng, N. Zhang, J. Seok, *Acc. Chem. Res.* **2018**, *51*, 273.
[7] J. Cabana, L. Monconduit, D. Larcher, M. R. Palacín, *Adv. Mater.* **2010**, *22*, E170.
[8] Y.-Y. Hu, Z. Liu, K.-W. Nam, O. J. Borkiewicz, J. Cheng, X. Hua, M. T. Dunstan, X. Yu, K. M. Wiaderek, L.-S. Du, K. W. Chapman, P. J. Chupas, X.-Q. Yang, C. P. Grey, *Nat. Mater.* **2013**, *12*, 1130.
[9] Q. Li, H. Li, Q. Xia, Z. Hu, Y. Zhu, S. Yan, C. Ge, Q. Zhang, X. Wang, X. Shang, S. Fan, Y. Long, L. Gu, G.-X. Miao, G. Yu, J. S. Moodera, *Nat. Mater.* **2021**, *20*, 76.
[10] M. Keppeler, N. Shen, S. Nageswaran, M. Srinivasan, *J. Mater. Chem. A* **2016**, *4*, 18223.
[11] L. Zhang, H. B. Wu, X. W. D. Lou, *Adv. Energy Mater.* **2014**, *4*, 1300958.
[12] J. Tang, C. E. Z. Lugo, S. F. A. Guzmán, G. Daniel, V. G. Kessler, G. A. Seisenbaeva, V. G. Pol, *J. Mater. Chem. A* **2016**, *4*, 18107.
[13] L. Yang, Y. Wu, Y. Wu, W. Younas, J. Jia, C. Cao, *J. Energy Storage* **2019**, *23*, 363.
[14] Y. Jiang, D. Zhang, Y. Li, T. Yuan, N. Bahlawane, C. Liang, W. Sun, Y. Lu, M. Yan, *Nano Energy* **2014**, *4*, 23.
[15] F. Jiao, J. Bao, P. G. Bruce, **2007**, *10*, A264.
[16] J. Li, S. Hwang, F. Guo, S. Li, Z. Chen, R. Kou, Ke Sun, C.-J. Sun, H. Gan, A. Yu, E A. Stach, H. Zhou, D. Su, *Nat. Commun.* **2019**, *10*, 2224.
[17] D. McNulty, D. N. Buckley, C. O'Dwyer, *J. Solid State Electrochem.* **2016**, *20*, 1445.
[18] Y. Liu, L. Ren, X. Qi, L. Yang, J. Li, Y. Wang, J. Zhong, *J. Energy Chem.* **2014**, *23*, 207.
[19] J. B. Boland, R. Tian, A. Harvey, V. V. Mayoral, A. Griffin, D. V. Horvath, C. Gabbett, M. Breshears, J. Pepper, Y. Li, J. N. Coleman, *2D Mater.* **2020**, *7*, 035015.
[20] R. Tian, A. Griffin, M. McCrystall, M. Breshears, A. Harvey, C. Gabbett, D. V. Horvath, C. Backes, Y. Jing, T. Heine, S.-H. Park, J. Coelho, V. Nicolosi, M. Nentwig, C. Benndorf, O. Oeckler, J. N. Coleman, *Adv. Energy Mater.* **2021**, *11*, 2002364.
[21] R. Tian, M. Breshears, D. V. Horvath, J. N. Coleman, *ACS Nano* **2020**, *14*, 3129.
[22] L. Li, H. B. Wu, L. Yu, S. Madhavi, X. W. Loue, *Adv. Mater. Interfaces* **2014**, *1*, 1400050.
[23] T. R. Penki, S. Shivakumara, M. Minakshi, N. Munichandraiah, *Electrochim. Acta* **2015**, *167*, 330.
[24] K. Cao, L. Jiao, H. Liu, Y. Liu, Y. Wang, Z. Guo, H. Yuane, *Adv. Energy Mater.* **2015**, *5*, 1401421.
[25] L. Lv, M. Peng, L. Wu, Y. Dong, G. You, Y. Duan, W. Yang, L. He, X. Liu, *Nanoscale Res. Lett.* **2021**, *16*, 138.
[26] A. J. G. Zarbin, *Mater. Horiz.* **2021**, *8*, 1409.
[27] I. Robayo-Molina, A. F. Molina-Osorio, L. Guinane, S. A. M. Tofail, M. D. Scanlon, *J. Am. Chem. Soc.* **2021**, *143*, 9060.
[28] A. F. Molina-Osorio, D. Cheung, A. A. Stewart, M. Dossot, *J. Phys. Chem. C* **2020**, *124*, 6929.
[29] R. A. Lehane, A. Gamero-Quijano, S. Malijauskaite, A. Holzinger, M. Conroy, F. Laffir, A. Kumar, U. Bangert, K. Mcgourty, *J. Am. Chem. Soc.* **2022**, *144*, 4853.
[30] M. F. Suárez-Herrera, M. D. Scanlon, *Electrochim. Acta* **2019**, *328*, 135110.
[31] S. Wei, D. Di Lecce, J. Hassoun, *ACS Appl. Energy Mater.* **2021**, *4*, 8340.
[32] C. Wu, X. Li, W. Li, B. Li, Y. Wang, Y. Wang, M. Xu, L. Xing, *J. Power Sources* **2014**, *251*, 85.
[33] Q. Zhao, J. Liu, X. Li, Z. Xia, Q. Zhang, M. Zhou, W. Tian, M. Wang, H. Hu, Z. Li, W. Wu, H. Ning, M. Wu, *Chem. Eng. J.* **2019**, *369*, 215.
[34] Z. Zheng, P. Li, J. Huang, H. Liu, Y. Zao, Z. Hu, L. Zhang, H. Chen, M.-S. Wang, D.-L. Peng, Q. Zhang, *J. Energy Chem.* **2020**, *41*, 126.
[35] V. Vega-Mayoral, R. Tian, A. G. Kelly, A. Griffin, A. Harvey, M. Borrelli, K. Nisi, C. Backes, J. N. Coleman, *Nanoscale* **2019**, *11*, 6206.
[36] C. J. Zhang, S.-H. Park, O. Ronan, A. Harvey, A. S. Ascaso, Z. Lin, N. McEvoy, C. S. Boland, N. C. Berner, G. S. Duesberg, P. Rozier, J. N. Coleman, V. Nicolosi, *Small* **2017**, *13*, 1701677.
[37] D. Kong, X. Qiu, B. Wang, Z. Xiao, X. Zhang, R. Guo, Y. Gao, Q.-H. Yang, L. Zhi, *Sci. China Mater.* **2018**, *61*, 671.
[38] S.-H. Park, P. J. King, R. Tian, C. S. Boland, J. Coelho, C. Zhang, P. McBean, N. McEvoy, M. P. Kremer, D. Daly, J. N. Coleman, V. Nicolosi, *Nat. Energy* **2019**, *4*, 560.
[39] C. Gabbett, C. S. Boland, A. Harvey, V. Vega-Mayoral, R. J. Young, J. N. Coleman, *Chem. Mater.* **2018**, *30*, 5245.
[40] Y. Liu, X. He, D. Hanlon, A. Harvey, U. Khan, Y. Li, J. N. Coleman, *ACS Nano* **2016**, *10*, 5980.
[41] X. Tang, R. Jia, T. Zhai, H. Xia, *ACS Appl. Mater. Interfaces* **2015**, *7*, 27518.
[42] J.-S. Wei, J. Chen, H. Ding, P. Zhang, Y.-G. Wang, H.-M. Xiong, *J. Power Sources* **2017**, *364*, 465.
[43] M. D. Scanlon, E. Smirnov, T. J. Stockmann, P. Peljo, *Chem. Rev.* **2018**, *118*, 3722.
[44] A. N. J. Rodgers, S. G. Booth, R. A. W. Dryfe, *Electrochem. Commun.* **2014**, *47*, 17.
[45] P. S. Toth, S. J. Haigh, A. K. Rabiu, A. N. J. Rodgers, A. M. Rakowski, R. A. W. Dryfe, *J. Mater. Res.* **2015**, *30*, 2679.
[46] A. L. Barker, P. R. Unwin, *J. Phys. Chem. B* **2001**, *105*, 12019.
[47] A. P. Balan, S. Radhakrishnan, C. F. Woellner, S. K. Sinha, L. Deng, C. de los Reyes, B. M. Rao, M. Paulose, R. Neupane, A. Apte, V. Kochat, R. Vajtai, A. R. Harutyunyan, C.-W. Chu, G. Costin, D. S. Galvao, A. A. Martí, P. A. van Aken, O. K. Varghese, C. S. Tiwary, A. M. M. R. Iyer, P. M. Ajayan, *Nat. Nanotechnol.* **2018**, *13*, 602.
[48] X. Liu, W. Si, J. Zhang, X. Sun, J. Deng, S. Baunack, S. Oswald, L. Liu, C. Yan, O. G. Schmidt, *Sci. Rep.* **2014**, *4*, 7452.
[49] V. Nicolosi, M. Chhowalla, M. G. Kanatzidis, m. S. Strano, J. N. Colemane, *Science* **2013**, *340*, 1226419.
[50] Y. Hernandez, V. Nicolosi, M. Lotya, F. M. Blighe, Z. Sun, S. De, I. T. Mcgovern, B. Holland, M. Byrne, Y. K. Gun'Ko, J. J. Boland, P. Niraj, G. Duesberg, S. Krishnamurthy, R. Goodhue, J. Hutchison, V. Scardaci, A. C. Ferrari, J. N. Coleman, *Nat. Nanotechnol.* **2008**, *3*, 563.
[51] J. N. Coleman, M. Lotya, S. D. Bergin, P. J. King, U. Khan, K. Young, A. Gaucher, S. De, R. J. Smith, I. V. Shvets, S. K. Arora, G. Stanton, H.-Y. Kim, K. Lee, G. T. Kim, G. S. Duesberg, T. Hallam, J. J. Boland, J. J. Wang, J. F. Donegan, J. C. Grunlan, G. Moriarty, A. Shmeliov, R. J. Nicholls, J. M. Perkins, E. M. Grieveson, K. Theuwissen, D. W. Mccomb, P. D. Nellist, V. Nicolosi, *Science* **2011**, *331*, 568.

[52] H. Kaur, R. Tian, A. Roy, M. Mccrystall, D. V. Horvath, G. L. Onrubia, R. Smith, M. Ruether, A. Griffin, C. Backes, V. Nicolosi, J. N. Coleman, *ACS Nano* **2020**, *14*, 13418.
[53] C. Backes, R. J. Smith, N. McEvoy, N. C. Berner, D. Mccloskey, H. C. Nerl, P. J. King, T. Higgins, D. Hanlon, N. Scheuschner, J. Maultzsch, L. Houben, G. S. Duesberg, J. F. Donegan, V. Nicolosi, J. N. Coleman, *Nat. Commun.* **2014**, *5*, 4576.
[54] A. Harvey, C. Backes, J. B. Boland, X. He, A. Griffin, B. Szydlowska, C. Gabbett, J. F. Donegan, J. N. Coleman, *Nat. Commun.* **2018**, *9*, 4553.
[55] Y. P. He, Y. M. Miao, C. R. Li, S. Q. Wang, L. Cao, S. S. Xie, G. Z. Yang, B. S. Zou, C. Burda, *Phys. Rev. B* **2005**, 71.
[56] C. Backes, D. Campi, B. M. Szydlowska, K. Synnatschke, E. Ojala, F. Rashvand, A. Harvey, A. Griffin, Z. Sofer, N. Marzari, J. N. Coleman, *ACS Nano* **2019**, *13*, 7050.
[57] T. Chen, H. Kaur, M. McCrystall, R. Tian, A. Roy, R. Smith, D. V. Horvath, J. Maughan, B. Konkena, M. Venkatesan, K. Synnatschke, T. Carey, J. Liu, J. Pepper, R. Zhang, C. Backes, V. Nicolosi, H. Xia, J. N. Coleman, *FlatChem* **2022**, *33*, 100360.
[58] C. (J.) Zhang, M. Liang, S.-H. Park, Z. Lin, L. Wang, A. Pakdel, J. Boland, O. Ronan, N. McEvoy, B. Lu, Y. Wang, Y. Xia, J. N. Coleman, V. Nicolosi, *Energy Environ. Sci.* **2020**, *13*, 2124.
[59] M. Chen, J. Liu, D. Chao, J. Wang, J. Yin, J. Lin, H. Jin Fan, Z. X. Shen, *Nano Energy* **2014**, *9*, 364.
[60] Z. Wang, D. Luan, S. Madhavi, Y. Hu, X. W. (D.) Lou, *Energy Environ. Sci.* **2012**, *5*, 5252.
[61] M. R. Palacín, *Chem. Soc. Rev.* **2009**, *38*, 2565.
[62] Y. Chai, X. Wang, Y. Yu, X. Shi, Q. Zhang, N. Wang, *Int. J. Energy Res.* **2019**, *43*, 6045.
[63] D. Larcher, C. Masquelier, D. Bonnin, Y. Chabre, V. Masson, J.-B. Leriche, J.-M. Tarascon, *J. Electrochem. Soc.* **2003**, *150*, A133.
[64] H. Sun, G. Xin, T. Hu, M. Yu, D. Shao, X. Sun, J. Lian, *Nat. Commun.* **2014**, *5*, 4526.
[65] A. Ponrouch, P.-L. Taberna, P. Simon, M. R. Palacín, *Electrochim. Acta* **2012**, *61*, 13.
[66] J. W. Choi, J. Mcdonough, S. Jeong, J. S. Yoo, C. K. Chan, Y. Cui, *Nano Lett.* **2010**, *10*, 1409.
[67] Y.-S. Hu, Y.-G. Guo, W. Sigle, S. Hore, P. Balaya, J. Maier, *Nat. Mater.* **2006**, *5*, 713.
[68] M. V. Reddy, T. Yu, C. H. Sow, Z. X. Shen, C. T. Lim, G. V. S. Rao, B. V. R. Chowdari, *Adv. Funct. Mater.* **2007**, *17*, 2792.
[69] J. Wang, H. Zhou, J. Nanda, P. V. Braun, *Chem. Mater.* **2015**, *27*, 2803.
[70] S. Fleischmann, J. B. Mitchell, R. Wang, C. Zhan, D.-E. Jiang, V. Presser, V. Augustyn, *Chem. Rev.* **2020**, *120*, 6738.
[71] A. J. Bard, L. R. Faulkner, *Electrochemical Methods Fundamentals and Applications*, John Wiley and Sons, New York **2001**.
[72] D.-W. Chung, M. Ebner, D. R. Ely, V. Wood, R. E. García, *Modell. Simul. Mater. Sci. Eng.* **2013**, *21*, 074009.
[73] F. L. E. Usseglio-Viretta, A. Colclasure, A. N. Mistry, K. P. Y. Claver, F. Pouraghajan, D. P. Finegan, T. M. M. Heenan, D. Abraham, P. P. Mukherjee, D. Wheeler, P. Shearing, S. J. Cooper, K. Smith, *J. Electrochem. Soc.* **2018**, *165*, A3403.
[74] D. V. Horvath, R. Tian, V. Nicolosi, J. N. Coleman, *ACS Appl. Energy Mater.* **2020**, *3*, 10154.
[75] D. V. Horváth, R. Tian, C. Gabbett, V. Nicolosi, J. N. Coleman, *J. Electrochem. Soc.* **2022**, *169*, 030503.
[76] S.-H. Park, R. Tian, J. Coelho, V. Nicolosi, J. N. Coleman, *Adv. Energy Mater.* **2019**, *9*, 1901359.
[77] R. Tian, N. Alcala, D. V. Horvath, A. J. Griffin, Y. Zhang, V. Nicolosi, J. N. Coleman, *ACS Appl. Energy Mater.* **2020**, *3*, 2966.
[78] R. Tian, S.-H. Park, P. J. King, G. Cunningham, J. Coelho, V. Nicolosi, J. N. Coleman, *Nat. Commun.* **2019**, *10*, 1933.
[79] J. K. Shon, H. S. Lee, G. O. Park, J. Yoon, E. Park, G. S. Park, S. S. Kong, M. Jin, J.-M. Choi, H. Chang, S. Doo, J. M. Kim, W.-S. Yoon, C. Pak, H. Kim, G. D. Stucky, *Nat. Commun.* **2016**, *7*, 11049.